CrystEngComm

HIGHLIGHT

View Article Online
View Journal | View Issue

Cite this: *CrystEngComm*, 2018, **20**, 2886

Atomic force microscopy imaging of classical and nonclassical surface growth dynamics of calcium orthophosphates

Meng Li,[a] Lijun Wang *[a] and Christine V. Putnis[bc]

Received 5th December 2017,
Accepted 21st March 2018

DOI: 10.1039/c7ce02100c

rsc.li/crystengcomm

Calcium orthophosphates (Ca-Ps) have long been the focus of extensive research due to their significance as inorganic phases of biomineral bones and teeth and the primary constituent of the majority of pathological calcified tissues. The utilization of atomic force microscopy (AFM) as an *in situ* imaging technique is to probe nanoscale and even near-molecular processes during Ca-P crystallization and unravel the underlying modulation mechanisms of biological molecules. According to the solubility defined as the equilibrium solute concentration for Ca-P growth, we first review classical crystallization mechanisms of brushite (DCPD) and the role of step-specific interactions, providing a context for interpreting the changes of step movement velocities and visualizing the modification of the growth hillock (spiral growth) morphology and the step features on a DCPD crystal surface in the presence of growth modulators using AFM. A nonclassical crystallization pathway for octacalcium phosphate (OCP) and hydroxyapatite (HAP) is then reviewed so that the effects of biomolecules, such as amelogenin proteins on tooth enamel formation, are set in a broader biomineralization context. Finally, we show how recent advances using AFM-based single molecule force spectroscopy (SMFS) have provided the energetic basis for probing the interactions between osteopontin (OPN) peptides and HAP to define a thermodynamic understanding of OPN roles in the growth of HAP at biomimetic cell membrane surfaces. These *in situ* AFM observations improve the fundamental understanding of the interfacial growth of Ca-P biominerals and their biomimetic substitute materials.

1. Introduction

Over 60 different biominerals found in various organisms have been extensively investigated, and as main mineralized tissues in bones and teeth,[1] the study of calcium orthophosphates (Ca-Ps) has attracted wide attention. Various Ca-P precursors are recognized and interact with biological molecules, and eventually crystallize into thermodynamically stable hydroxyapatite ($Ca_{10}(PO_4)_6(OH)_2$, HAP, $P6_3/m$ or $P2_1/b$ space group).[2] In these processes, complex intermediate phases, such as amorphous calcium phosphate ($Ca_xH_y(PO_4)_z{\cdot}nH_2O$, n = 3–4.5; 15–20% H_2O, ACP), brushite ($CaHPO_4{\cdot}2H_2O$, DCPD, Ia space group), and octacalcium phosphate ($Ca_8(HPO_4)_2(PO_4)_4{\cdot}5H_2O$, OCP, $P\bar{1}$ space group), may participate in the crystallization process.[3] Posner and Betts[4,5] reported that hydrated $Ca_9(PO_4)_6$ clusters (Posner's clusters) could be randomly agglomerated into spherical ACP particles, and Posner's clusters with a height of about 1.02 nm were observed *in situ* by atomic force microscopy (AFM) during a coupled process of calcium carbonate dissolution–calcium phosphate reprecipitation.[6] Also, constant composition (CC) nucle-

[a] *College of Resources and Environment, Huazhong Agricultural University, Wuhan 430070, China. E-mail: ljwang@hzau.edu.cn; Tel: +86 27 87288382*
[b] *Institut für Mineralogie, University of Münster, 48149 Münster, Germany*
[c] *Department of Chemistry, Curtin University, Perth, Western Australia 6845, Australia*

Lijun Wang

Lijun Wang completed his B.S. from China Agricultural University, Beijing, and his Ph.D. from Huazhong Agricultural University (HZAU), Wuhan. He collaborated with Dr. George Nancollas as a postdoctoral associate and research assistant professor at the State University of New York at Buffalo. He was also a postdoctoral fellow with Dr. James De Yoreo at Lawrence Berkeley National Laboratory. He is currently a Professor at the HZAU. His research focus is on the dynamics of biomineralization and geomineralization with an emphasis on crystallization of calcium phosphates and silica.

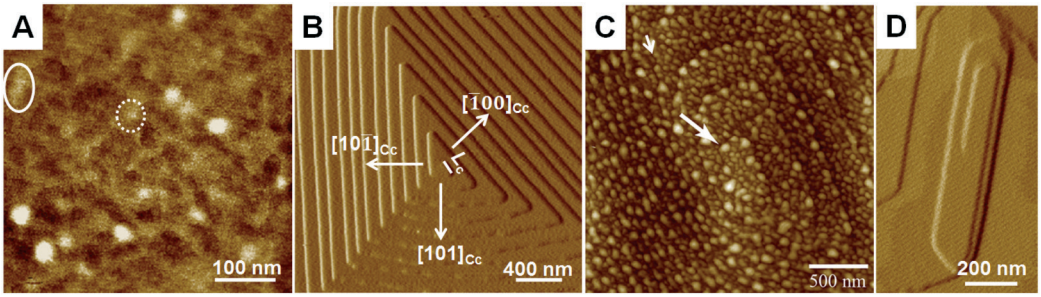

Fig. 1 AFM images of the surface features of several representative calcium orthophosphates showing (A) ACP nanoparticles on the HAP surface (shown by circles),[12] (B) a triangular growth hillock on the DCPD (010) face, (C) the coexistence of an asymmetric rectangular growth hillock and nanoparticles on the OCP surface,[28] and (D) a hexagonal growth hillock on the HAP (100) surface. Adapted with permission from ref. 12 and 28. Copyright 2016 American Chemical Society and 2015 Scientific Research Publishing.

ation revealed that the calcium-deficient amorphous phase-I ($Ca(HPO_4)_{1+x}\cdot nH_2O$, ACP-I) formed first, followed by dehydration and aggregation to form amorphous phase-II ($Ca(HPO_4)\cdot mH_2O$, ACP-II).[7] In addition, $Ca(\eta^2\text{-}PO_4^{3-})_2\cdot L_2$ (L = H_2O, $\eta^2\text{-}PO_4^{3-}$, where η^2 stands for the bidentate binding of the phosphate group)[8] and polymeric assemblies of $CaHPO_4/CaH_2PO_4^+$ ($\leq$14%) and $Ca(HPO_4)_3^{4-}/Ca(HPO_4)_2(H_2PO_4)^{3-}$ ($\geq$86%)[9] might also exist in the initial supersaturated solutions. The ion-association complexes of $[Ca(HPO_4)_3]^{4-}$ may aggregate and take up additional calcium ions from solution to form post-nucleation clusters of $[Ca_2(HPO_4)_3]^{2-}$ that subsequently precipitate as ACP.[9] *Ab initio* molecular dynamic simulations[10] elucidated that calcium was seven-coordinated by two water molecules, two bidentate phosphates and one monodentate phosphate to form $[Ca(\eta^2\text{-}HPO_4^{2-})(\eta^1\text{-}HPO_4^{2-})]^{4-}\cdot(H_2O)_2$ (η^1 stands for the monodentate binding of the phosphate group), and the calcium triphosphate prenucleation complexes were more thermodynamically stable than the isolated ions, dramatically reducing the nucleation barrier.[10] With the advent of high-resolution cryogenic transmission electron microscopy (HR-cryoTEM), Dey *et al.*[11] observed that nanoclusters with a height of 0.87 nm aggregated to form spherical ACP that eventually transformed into a stable crystalline phase. *In situ* AFM also observed that ACP formed during the initial surface growth of HAP under near physiological solution conditions (Fig. 1A).[12]

The ACP phase in physiological solution gradually transforms into a crystalline HAP phase. During the phase transformation, the dissolution and growth of different crystal surfaces are modulated by a variety of organic and inorganic molecules. As an *in situ* observation technique in solutions, AFM can capture the real-time dissolution and growth kinetics from the near-molecular scale to nanoscale.[12–14] Using AFM, the interaction between biomolecules and minerals can also be determined by tip-modified single molecule force spectroscopy (SMFS).[15–17] In this review, we summarize recent progress related to the surface growth dynamics of several Ca-P phases and their modulation by relevant biomolecules, providing fundamental clues to reveal the molecular mechanisms of Ca-P biomineralization and possible implications in the synthesis of biomimetic materials.

2. Relevant Ca-P phases used for AFM imaging

2.1. DCPD

DCPD has been proposed as an intermediate phase in *in vitro* formation of OCP and HAP and can be easily crystallized under neutral and acidic conditions, and it is often found in pathological calcification.[18] Since the DCPD {010} face is highly hydrated and has a relatively low interfacial energy,[19] {010} thus dominates the DCPD habit as thin plate-like crystals. Real-time *in situ* AFM imaging reveals the triangular spiral growth by measuring the spreading rates of three step directions of $[10\bar{1}]_{Cc}$, $[101]_{Cc}$ and $[\bar{1}00]_{Cc}$ (Fig. 1B), in which the $[\bar{1}00]_{Cc}$ steps have the slowest velocity.[19] The three steps are also easily observed in etch pits during the dissolution.[20–24]

2.2. OCP

OCP exhibits a significant biological role in the chemistry of bones and tooth enamel as it is the precursor phase of HAP.[25,26] The synthesized OCP crystallites typically show an elongated thin plate with a well-developed (100) face.[9,27] AFM observations show that growth hillocks (spiral growth) on the OCP (100) face exhibit an asymmetric rectangular shape with a monomolecular step height of about 2.0–2.5 nm (Fig. 1C),[28] close to 1.86 nm expected from the unit cell parameters and OCP symmetry.[28] This is consistent with Wu *et al.*'s measurements[29] of the monomolecular steps with an average height of 1.99 ± 0.06 nm. It is generally assumed that the crystal structure of OCP is an alternate stacking of apatitic and hydrated layers parallel to the (100) face.[25,30,31] The hydrated layer contains lattice water and less densely packed calcium and phosphate ions, and the apatitic layer in OCP is similar to the apatitic structure in HAP, exhibiting a hexagonal system crystal structure.[3,30,32] This similarity between OCP and HAP provides geometrically favorable conditions for the transformation of OCP to HAP by epitaxial growth, where the [001] and [010] axes for OCP are along the same directions as the $[000\bar{1}]$ and $[2\bar{1}\bar{1}0]$ axes for HAP, respectively.[33] During the transformation, water molecules can enter the hydration layers of OCP crystals *via* a hydrolysis reaction that accounts for the deprotonation of HPO_4^{2-} ions.[33] In this

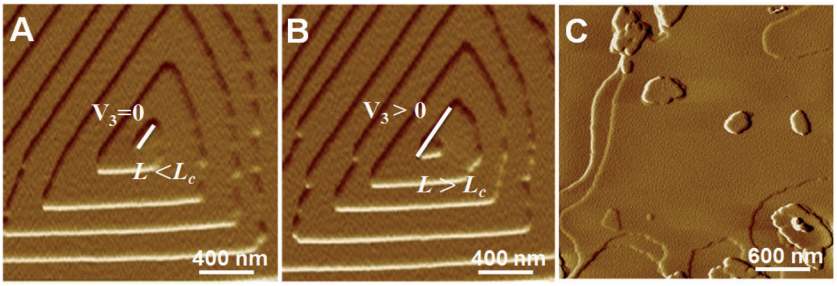

Fig. 2 AFM images showing classical crystallization pathways of DCPD. (A and B) Classical spiral growth occurs only when the step length (L) reaches its critical length (L_c) at relatively low supersaturations.[73] (C) 2D nucleation at relatively high supersaturation generates new steps resulting in rapid crystallization. Adapted with permission from ref. 73. Copyright 2015 American Chemical Society.

process, inorganic ions, such as CO_3^{2-}, F^-, Na^+ and K^+, can incorporate into the HAP lattice and thus have a considerable influence on the HAP physical and physicochemical properties.[25,34,35]

2.3. HAP

As the most thermodynamically stable phase of Ca-Ps, HAP exhibits a crystal structure of either monoclinic or hexagonal crystal phases,[36,37] and an *in vitro* transition from the monoclinic to a hexagonal phase occurs at higher temperatures.[38] However, hexagonal HAP crystals are generally found in biological apatites.[39] Taking into account that biomineralization usually occurs at physiological temperatures, this is probably due to the existence of hexagonal seed crystals, habit modifiers or water-insoluble bio-template molecules. Molecular dynamics simulations show that the surface energies of the side and basal surfaces of HAP in water are 0.42 and 0.66 J m^{-2}, respectively.[40] The growth of HAP is limited by the basal surface, leading to a prism morphology with six prismatic {100} surfaces and a basal (001) surface. For the hexagonal form, calcium ions are arranged symmetrically along the [010] direction and two parallel layers of phosphate ions are located at heights of 1/4 and 3/4 of the unit cell.[40] In addition, hydroxide ions are arranged along the *c*-axis, pointing to the opposite direction to the same column of adjacent hydroxyl,[40] resulting in the enhanced stability of the HAP crystal structure. Expectedly, the AFM images show that the growth hillocks on the (100) face exhibit a typical hexagonal morphology (Fig. 1D),[12] bound by six well-defined steps with an average height of 8.21 Å that matches the theoretical *d*-spacing height of 8.17 Å for the (100) face.[12] However, the steps of the relatively smooth HAP (001) surface are not easy to observe, mainly because the surface is covered with nanoparticles.[12,41]

3. Dynamics and mechanisms of the surface growth of Ca-Ps in pure solutions

3.1. Classical pathway of monomer addition

Classical crystal growth is based on monomer-by-monomer addition of simple chemical species of ions or molecules described using a terrace–ledge–kink (TLK) model.[42,43] According to whether the crystal surface contains dislocations, defects and other active sites, the crystal grows by two modes of spiral growth and two-dimensional island growth.[42,43] When the crystal surface pre-exists with active sites and is exposed to relatively low supersaturated solutions, the attachment of monomers at active sites leads to advancement of steps, and the inherent screw dislocations in crystal lattices are responsible for the nonterminating steps, exhibiting the spiral growth pathway. It has been established that both DCPD[23,24] and HAP[12] can grow in a spiral form. Due to the relatively high solubility of DCPD ($-\log(K_{sp})$ = 6.59, 25 °C),[3] the synthesized DCPD crystallites at room temperature can be up to millimeter sizes and are large enough for spiral growth to be observed *in situ* by AFM. According to classical surface growth mechanisms, the calcium and phosphate ions attach to the crystal surface, incorporate into the lattice and become a part of the crystal, involving various energy barriers including volume diffusion, dehydration, surface diffusion, incorporation of growth units into the crystal structure, and removal of the latent heat of crystallization.[44–48] It has been suggested that dehydration is the main limiting process for the advancement of the DCPD steps,[44,45] whereas the incorporation of ions or molecules into the crystal structure determines the velocities of the surface steps of HAP.[47]

As driving forces (the activity difference of solute species) are lower than the critical value of surface nucleation, the step advancement rate R for the (010) face of DCPD is given by

$$R = R_a - R_d = \upsilon h/W = \Omega\beta(c - c_e)h/W \quad (1)$$

where R_a and R_d are the attachment and detachment rates for solute species, respectively; υ is the step speed; h is the monomolecular step height of DCPD (0.76 nm);[24] W is the terrace width; Ω is the volume per growth unit (6.16×10^{-23} cm^3) in the DCPD crystal;[49] β is the step kinetic coefficient; c and c_e are the bulk and equilibrium concentrations of the growth units, respectively. The magnitude of β is controlled by two primary factors, including the density of kink sites along the step and the net probability of attachment of solute species to a growth site.[50] Thus, β is the key parameter to

understand the activation energy ΔG for the attachment of solute species to the step edge,

$$\beta = bv\exp(-\Delta G/kT) \quad (2)$$

where b is the lattice spacing and v is the frequency of vibration of atoms on the surface. According to eqn (2), we can calculate ΔG by measuring the value of β at a series of temperatures and predict that the additives in supersaturated solutions essentially affect the step propagation, terrace width and shape of spirals by changing the activation barrier. Moreover, the degree of supersaturation, pH, and ionic strength will also exert different influences on the activation barrier.[3,51]

Specifically, new steps of the triangular DCPD growth hillocks will be generated constantly only if the $[\bar{1}00]_{Cc}$ step exceeds its critical length L_c (Fig. 2A and B). L_c arises from the competition between the chemical potential and the step-edge energy.[46,49] Transferring growth units from the solution phase to the solid phase reduces the energy of the system, while additional new step-edges will increase the energy of the system. Thus, the total change in the free energy of the system is expressed as

$$\frac{\Delta G}{\Delta x_2} = -m\Delta\mu + hb_2\gamma_{step} \quad (3)$$

where m is the number of growth units added to the step, $\Delta\mu$ is the change in chemical potential per growth unit, b_2 is the length of the newly formed step-edge and γ_{step} is the step-edge free energy in units of energy per area as $\gamma_{step} = \gamma_{edge}/h$.[19] Taking into account that the step length is relevant to the number of growth units and the dimension of a growth unit parallel to the step b_1, $L = mb_1$, we can solve eqn (3) for

$$L_c = \frac{b_1 b_2 h\gamma_{step}}{\Delta\mu} = \frac{\Omega\gamma_{step}}{\Delta\mu} \quad (4)$$

when $\Delta G/\Delta x_2$ approaches zero, where the chemical potential $\Delta\mu = KT\ln S$ and S is the supersaturation ratio.[19]

Another key factor for the terrace width also determines the rate of crystal growth, as shown in eqn (1).[52] For a spiral with N sides, the time required for the $(i+1)$th step to reach its own critical length is $L_{C_{i+1}}\sin(a_{i,i+1})/v_i$,[43] thus, the terrace width can be expressed by[43,53]

$$W_i = v_i\sum_{i=1}^{n}\frac{L_{c_i}\sin(\alpha_{i,i+1})}{v_{i+1}} \quad (5)$$

where $a_{i,i+1}$ is the angle between the ith and the $(i+1)$th step. The solute species can either directly attach from the solution to kink sites or first adsorb on terraces, followed by surface diffusion and incorporation into the kink sites.[48] The terrace forms a two dimensional (2D) space for the surface diffusion of adsorbed solute species.[48,54] It has been established that closely spaced steps move significantly slower than well-separated steps,[48] because the step velocity considerably depends on the characteristic length of surface diffusion, λ. when $W \geq 2\lambda$, the step speed is independent of the terrace width; when $W \leq 2\lambda$, the step speed is positively correlated with the terrace width that[48]

$$\frac{\sigma}{v} = \frac{h\Lambda\Lambda_s}{\lambda^2\Omega c_e D} + \frac{\Lambda}{\Omega c_e D}\frac{h}{W} \quad (6)$$

where Λ and Λ_s are the resistance for adsorption from the bulk solution to the crystal surface and incorporation into kink sites from the surface, respectively. When $W \leq 2\lambda$, with the increase of W, the crystal growth rate decreases although the step speed increases; when $W \geq 2\lambda$, with the increase of W, the step speed is always at the maximum, and the crystal growth rate shows a downward trend.[48] For DCPD, the step spacing is always larger than 2λ in growth from most supersaturated solutions, thus the additives can modulate the DCPD growth by altering the terrace width. The above discussed spiral growth mode is based on stacking faults at inherent dislocations; without a nonterminating step source, any pre-existing steps will eventually grow out to the edge of the crystal leaving a featureless terrace.[44]

Another pathway to generate new steps and kinks is where growth units adsorb onto the crystal surface and subsequently

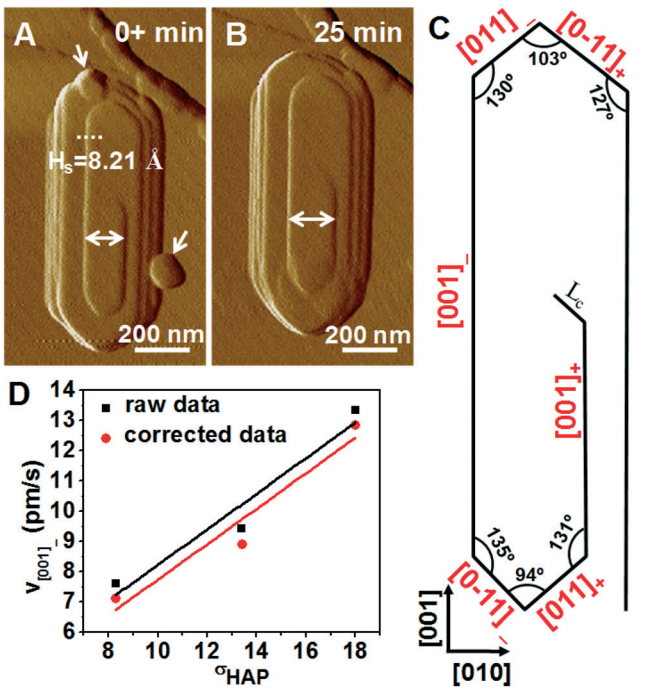

Fig. 3 AFM imaging of classical spiral growth of HAP and quantitative determination of step growth rates.[12] (A and B) AFM deflection images of the propagation of a hexagonal growth hillock on the HAP (100) surface at σ_{HAP} = 18. The white dotted line and arrows show the monomolecular step height of 8.21 Å and initially formed particles in (A), respectively. (C) Schematic of the corresponding spiral step with six unique orientations. (D) Measured step speed along the [001]_ step direction as a function of different supersaturations. Adapted with permission from ref. 12. Copyright 2016 American Chemical Society.

diffuse and aggregate into 2D nuclei. The formation of a nucleus must overcome a certain thermodynamic energy barrier, *i.e.*, only when the nucleus reaches its critical size, it will spontaneously grow. Based on the classic Gibbs–Thomson (G–T) effect, the critical radius is given by $r_c = 2\Omega\gamma_{SL}/\Delta\mu$, where γ_{SL} is the solid–liquid interfacial energy.[44] At relatively low supersaturation, the probability of forming the critical nucleus is low because of the large nucleation free energy barrier; the crystal grows by monomer addition to kink sites and step edges (Fig. 2A and B). With an increase in supersaturation, the number of nucleated particles increases with the reduction of the radius of the critical nucleus and the free energy barrier,[55,56] and consequently the growth pathway for DCPD changes from monomer addition to 2D nucleation (Fig. 2C). It has been estimated that the kink energy for DCPD is 2.5 k_BT from interfacial energy measurements.[57] When the supersaturation increases until the free energy barrier is comparable with k_BT, the solution will undergo spinodal decomposition,[58] at which point the nucleated particles significantly increase in number with subsequent collision and coalescence into larger particles. The successive stacking of 2D nuclei remarkably increases the growth rate of DCPD, therefore showing a non-linear relationship between the crystal growth rate and the supersaturation, $R = k\sigma^n$ $(n > 1)$.[59]

3.2. Nonclassical pathway of nanoparticle attachment

Crystal solubility determines the adsorption rate of particles onto a surface as well as the relative contributions of the pathway of monomer addition and nanoparticle attachment.[44,60] As the solubility of HAP ($-\log(K_{sp})$ = 116.8, 25 °C) is very low compared to that of DCPD, the rates of monomer-by-monomer addition are thus very low (Fig. 3).[12] The calculated step kinetic coefficient β for the $[001]_-$ step is 1.50 × 10^{-4} cm s^{-1} (Fig. 3D),[12] which is almost two orders of magnitude smaller than those of DCPD steps.[19] As a consequence, the relatively low value of β includes a large activation energy for addition of a solute molecule into a HAP crystal structure.[12] Previous results have confirmed that once the crystal solubility drops from molar levels to submicromolar levels,

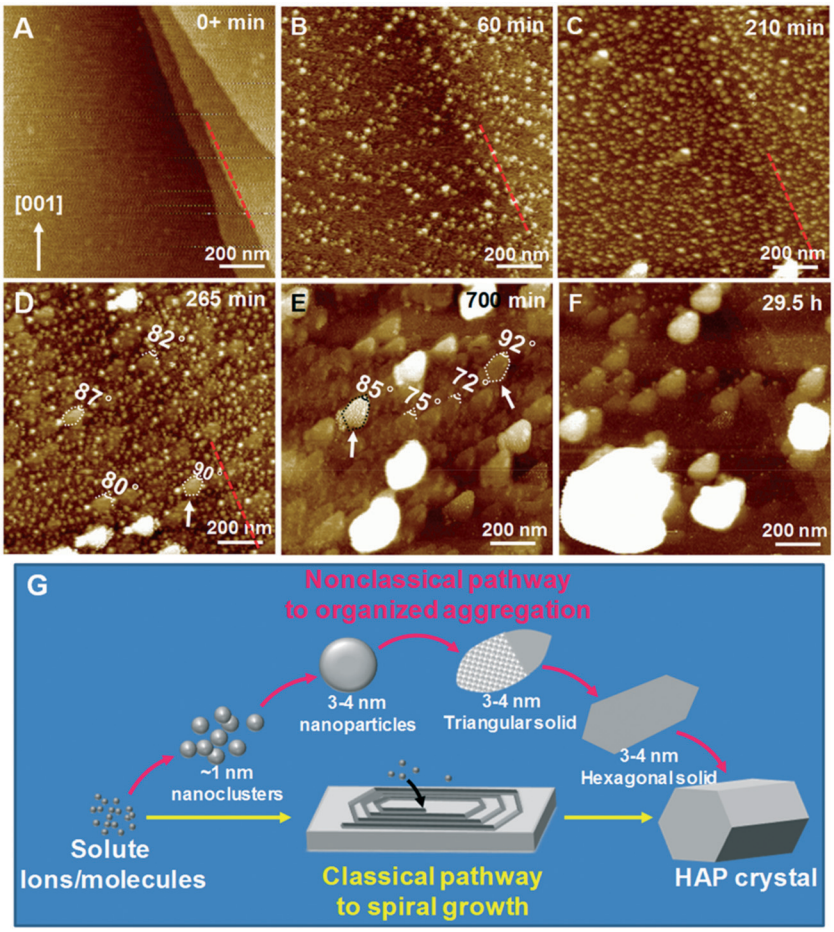

Fig. 4 Nonclassical crystallization of HAP by particle attachment.[12] (A–F) A sequence of AFM height images taken in the ScanAsyst mode with long imaging times of about 30 h showing the growth of HAP crystals by nanoparticle attachment and morphology evolution from nanoclusters/nanoparticles to triangular and hexagonal solid on the HAP (100) surface. (G) A schematic illustration of the pathways for HAP crystallization by attachment of different size particles from monomeric species to hexagonal solids. Adapted with permission from ref. 12. Copyright 2016 American Chemical Society.

the rates of monomer addition drop by a factor of ~10^{10} at equivalent values of supersaturation.[44,60] In fact, a supersaturated HAP solution already contains a distribution of monomers, complexes and clusters,[9,12,41] thus a particle-mediated growth pathway is energetically favorable and dominates HAP crystallization. Crystallization by nanoparticle attachment greatly improves the growth rate of insoluble Ca-Ps such as OCP[29] and HAP.[12] Through the Brownian motion in supersaturated HAP solution, pre-nucleation Ca-P clusters aggregate even below the critical nucleation conditions.[9] Crystallization of a stable HAP phase eventually occurs through either the aggregation of post-nucleation clusters or multistep phase evolution of complex metastable nanoparticles.[60] By long-term AFM imaging (about 30 h) of HAP (100) surface growth under constant supersaturated conditions (Fig. 4),[12] we observed that the small amorphous nanoparticles (1.0 nm or 3.0–4.0 nm in height) can form larger ordered hexagonal particles (3.0–4.0 nm in height) that transform into an intermediate phase through dissolution–recrystallization,[11,12] although crystallization by nanoparticle attachment is difficult to be distinguished solely by the external morphology because molecular or cluster addition, coarsening, and recrystallization can subsequently obliterate characteristic signatures.[60–63] Finally, a classical growth pathway of monomer-by-monomer addition and a nonclassical particle attachment pathway can co-exist during HAP surface crystallization (Fig. 4G).[12]

4. The role of additives

Crystal growth is controlled by both thermodynamic and kinetic factors, and the crystal surface with minimum free energy is preferentially expressed with the slowest growth rate and largest surface area.[44] Furthermore, the number of screw dislocations and the dimension of the step source distribution on a crystal surface have a considerable influence on the rate of crystal growth.[64] To some extent, the introduction of additives can change the crystal surface energy, altering the crystal morphology and even providing new dislocation sources to modulate the dynamics of the surface spiral growth and/or particle attachment. The additives can bind to step edges and/or terraces to affect the advancement of steps and/or step density,[44] or surface nucleation kinetics. The mechanisms by which additives regulate surface growth include step pinning, incorporation, and kink blocking.[44] Recent research has shown that a specific inhibitor of hydroxycitrate has a strong binding energy with mineral surfaces by inducing localized strain to dissolve the crystal even under supersaturated conditions.[65] Moreover, background electrolytes also have a considerable influence on the kinetics of crystal growth.[66]

4.1. Step pinning

The classic Cabrera–Vermilyea (C–V) model of step pinning explains inhibition of the DCPD surface growth kinetics by phosphorylated osteopontin (OPN) peptides as observed

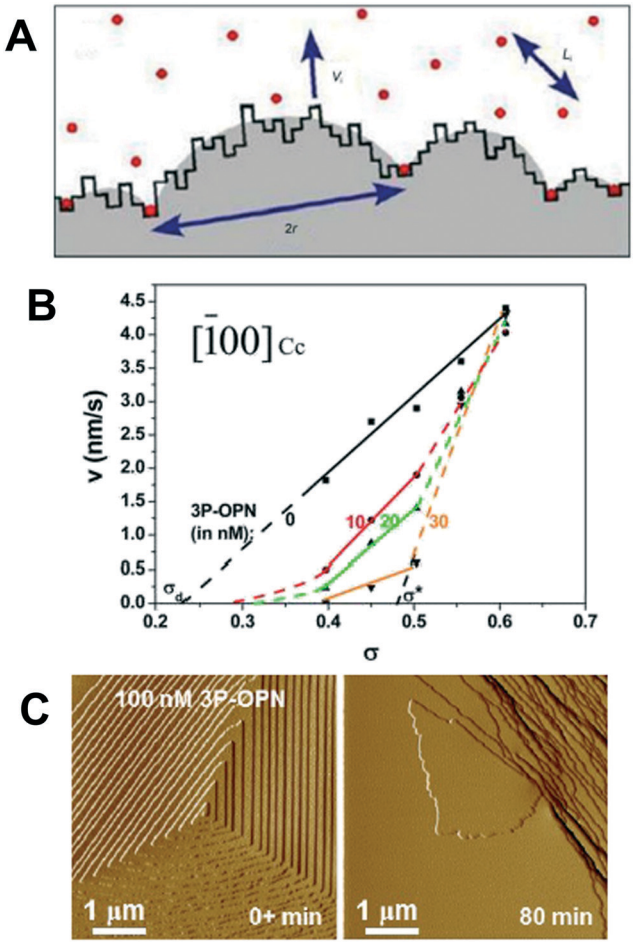

Fig. 5 Effect of 3P-OPN on the DCPD surface growth. (A) Schematic diagram of C–V model.[69] (B and C) The interaction of 3P-OPN-bearing solutions with a DCPD surface showing the $[\bar{1}00]_{Cc}$ step kinetics are consistent with the classic C–V model of step pinning, that is, there exhibits a dead zone where no growth occurs below σ_d.[24] Adapted with permission from ref. 24 and 69. Copyright 2009 and 2014 American Chemical Society.

by *in situ* AFM observations.[24] According to the C–V model, OPN peptides (circles in Fig. 5A) adsorb onto the steps through stronger competitiveness with solute species and roughen and inhibit the step movement as stoppers (Fig. 5A).[67–69] In essence, the C–V model involves two important parameters of average inhibitor spacing, L_i and step critical radius, r_c.[68] The step curvature is determined by L_i,[69] and the retardant effect on step advancement is explained by the G–T effect: as $L_i < Gr_c$ (G is dependent on the geometry of the crystal lattice[70,71]), the step is at a thermodynamically stable state and appears to cease moving.[71] A "dead zone" is created over a supersaturation range up to σ_d where no growth occurs (Fig. 5B). The critical impurity separation is actually an upper limit to block step movement.[68,70,72] For $L_i \geq Gr_c$, the C–V model successfully predicts the preferential adsorption behavior of 3P-OPN onto the DCPD $[\bar{1}00]_{Cc}$ step[24] as its velocity is given by $v_i = v_0(1 - GBr_cC_i^{0.5})$, where v_0 is the step velocity in a pure system, B is a proportionality coefficient related

to geometric factors, sticking probability, and the inhibitor lifetime.[71] 3P-OPN preferentially binding to the $[\bar{1}00]_{Cc}$ step instead of to the other two steps results in a change in the hillock shape (Fig. 5B and C). Considering selective and step-specific adsorption, the revised C–V model is appropriate for describing the action of 3P-OPN-regulated DCPD surface growth:

$$\frac{R_i}{R_0} = \frac{2}{3},\ L_i < Gr_c \tag{7}$$

$$\frac{R_i}{R_0} = 1 - \frac{1}{3}GBr_cC_i^{0.5},\ L_i \geq Gr_c \tag{8}$$

Thus, at sufficiently high 3P-OPN levels and low supersaturation, the growth of $[\bar{1}00]_{Cc}$ steps ceases and the surface growth rate for a DCPD (010) surface will be 2/3 of the growth rate in a pure solution (without additives).

4.2. Step density and interface energy

Recent studies on 13-mer amelogenin's C-terminus (13-mer Amel) has shown that peptides do not obviously roughen step-edges of DCPD and change step speeds, but the terrace width is increased at low peptide concentrations, that is the decrease in step density.[73] As shown in Fig. 6A 1 nM 13-mer Amel peptides modify the terrace width in the order $[10\bar{1}]_{Cc} \approx [101]_{Cc} > [\bar{1}00]_{Cc}$ due to the anisotropic modification of step energies.[73] Modifying the free energies of the step edges, γ_{step} (ref. 23 and 73) corresponds to a change of the interfacial free energy at a solid–liquid interface, γ_{SL}, which represents the mean value for γ_{step} of all crystal-face-step energies.[23,24] It is difficult to directly measure γ_{SL},[74] and the surface free energy in air, $\gamma_{S\text{-}air}$, but calculation by static contact angle measurement can serve as a rough proxy for γ_{SL}.[74] $\gamma_{S\text{-}air}$ points out the hydrophilicity of the substrate and larger $\gamma_{S\text{-}air}$ correlates with smaller γ_{SL}, *i.e.*, surfaces with a large amount of charge preferentially interact with polar water molecules.[74] Indeed, low concentrations of 13-mer Amel peptides will decrease $\gamma_{S\text{-}air}$ after adsorption onto the DCPD surface (Fig. 6B) and increase γ_{SL}.[73] An obvious increase of the terrace width highlights a thermodynamic mechanism of the interfacial energy control following the addition of 13-mer Amel peptides.

4.3. Other factors influencing the role of additives

Additives can block kinks or interfere with the ion hydration state to inhibit or accelerate growth.[44,75] For the nonclassical

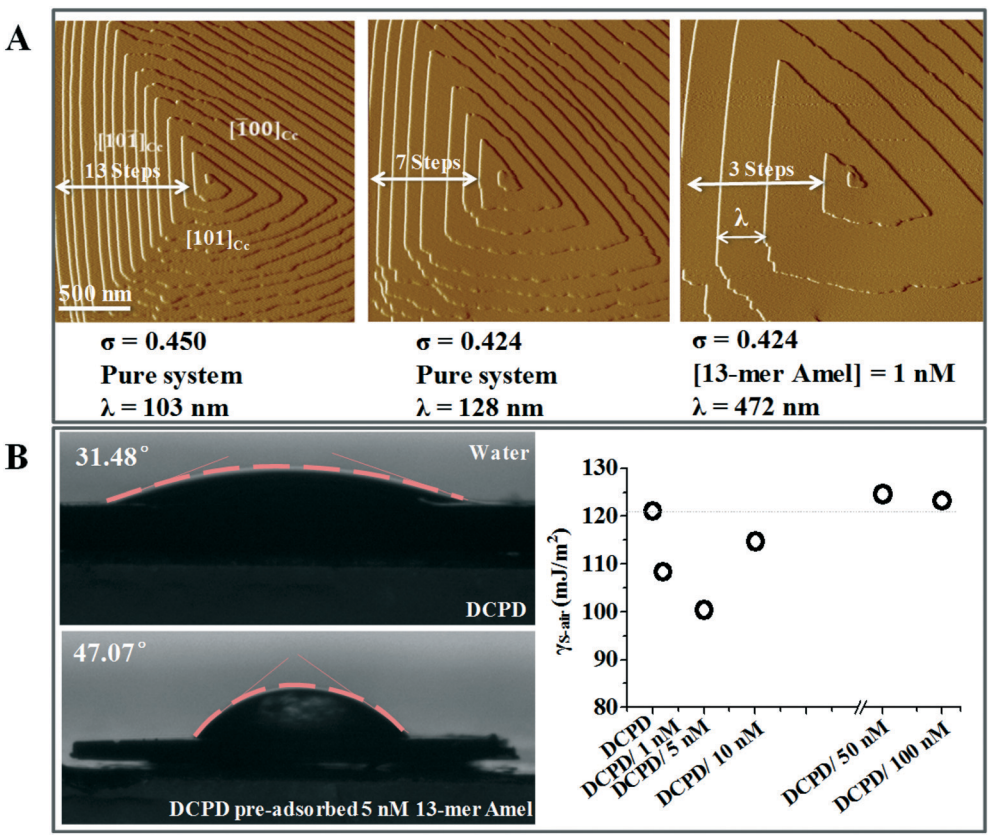

Fig. 6 Effects of 13-mer Amel peptides on step density and interfacial energies at the DCPD–water interface.[73] (A) AFM images showing the effect of 13-mer Amel peptides and supersaturation on the terrace width of a DCPD growth hillock. (B) Surface free energy of the DCPD substrates pre-adsorbing various concentrations of 13-mer Amel peptides determined by the static contact angle method. Adapted with permission from ref. 73. Copyright 2015 American Chemical Society.

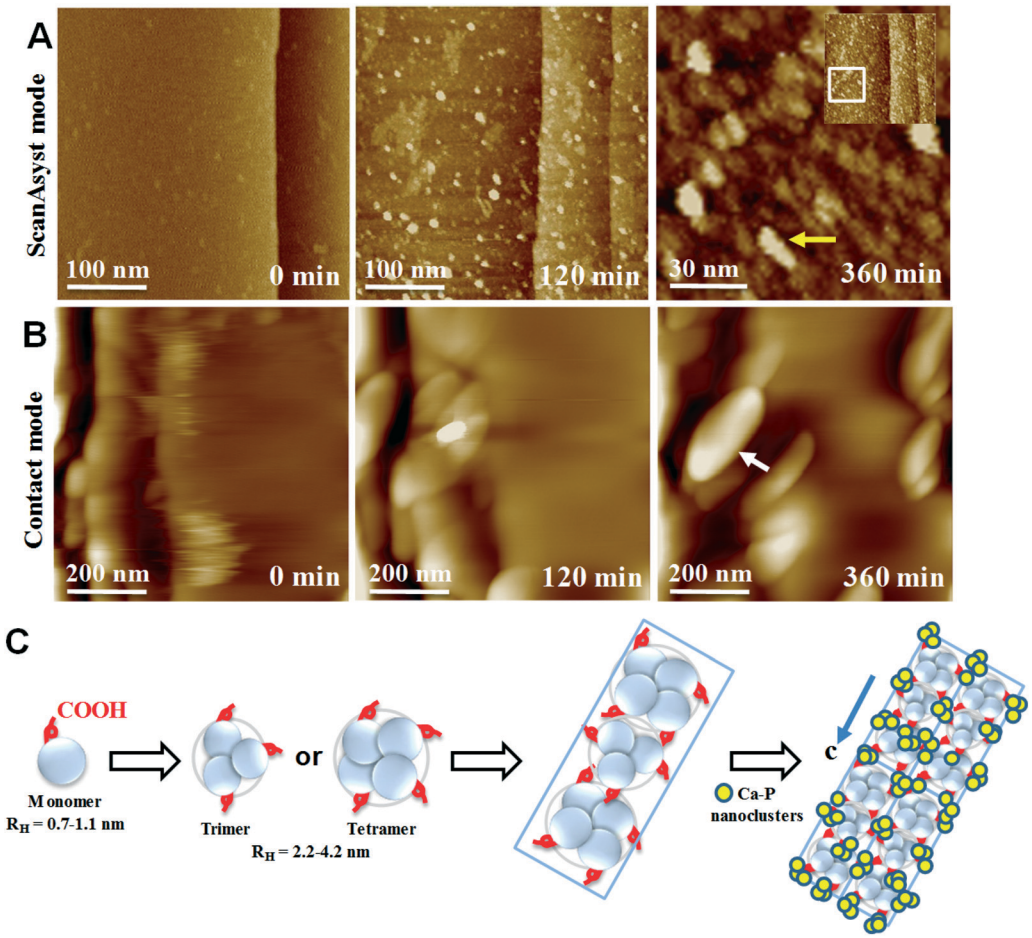

Fig. 7 Growth of an OCP crystal by particle attachment on the OCP (100) surface in the presence of Amel's C-terminal peptides.[29] AFM height images taken in (A) ScanAsyst mode (σ = 1.77) and (B) contact mode (σ = 1.86) showing the formation of elongated Ca-P nanoparticles in the presence of 50 nM Amel's C-terminal peptides after 360 min of surface nucleation and growth. (C) A schematic diagram of self-assembled Amel's C-terminal peptides to direct and template elongated OCP crystallization. Adapted with permission from ref. 29. Copyright 2017 American Chemical Society.

nanoparticle attachment mechanism, some additives, such as Amel that constitutes more than 90% of the total proteins found in the extracellular matrix in developing tooth enamel, can bind Ca-P nanoparticles and induce the formation of elongated OCP nanorods (Fig. 7).[29] The observed phenomenon is further analyzed and rationalized through fluorescence imaging and SMFS determination.[29] This is consistent with the role of citrate that covers about 1/6 (1 molecule per 4 nm^2)[76] of the available HAP surface area in bones and plays a dual role in the HAP surface growth:[12] inducing oriented adsorption of nanoclusters and nanoparticles along the HAP *c*-axis and stabilizing Ca-P clusters for a long time. The alignment of citrate on HAP is the same as that of the collagen fibers in bones, therefore contributing to the formation of elongated apatite. Finally, we need to mention that certain additives may incorporate within the resulting Ca-P single crystals and modify their properties.[77] Co-precipitation of mineral phases in the presence of additives was recently confirmed to be an effective strategy to produce composite single crystals with tunable mechanical, optical, or electric properties.

5. Biomolecule–mineral interactions at the single-molecule level

Nucleation and growth kinetics and the final crystal morphology largely depend on the strength of protein– or peptide–mineral surface interactions. The advent of AFM-based SMFS in fluid medium enabled information to be acquired about inter- and intra-molecular bonding and quantifying the free energy of biomolecule–mineral binding.[15,78] Following tip functionalization (Fig. 8A), one side of the crosslinker is immobilized on the apex of an AFM tip and the other side reacts with protein or peptide.[17] Different methods have been reported to functionalize the AFM tip, and one commonly used method is the linking of the N-terminal amine or lysine residues of the protein or peptide with gold-coated silicon nitride tips which are presorbed with a heterobifunctional cross-linker, LC-SPDP.[17] This process involves nucleophilic attack of deprotonated primary amines of protein or peptide with an *N*-hydroxysuccinimide ester of the bifunctional linker.[17] The modified tip is forced to be repeatedly in contact with the mineral substrate to obtain a series of force–

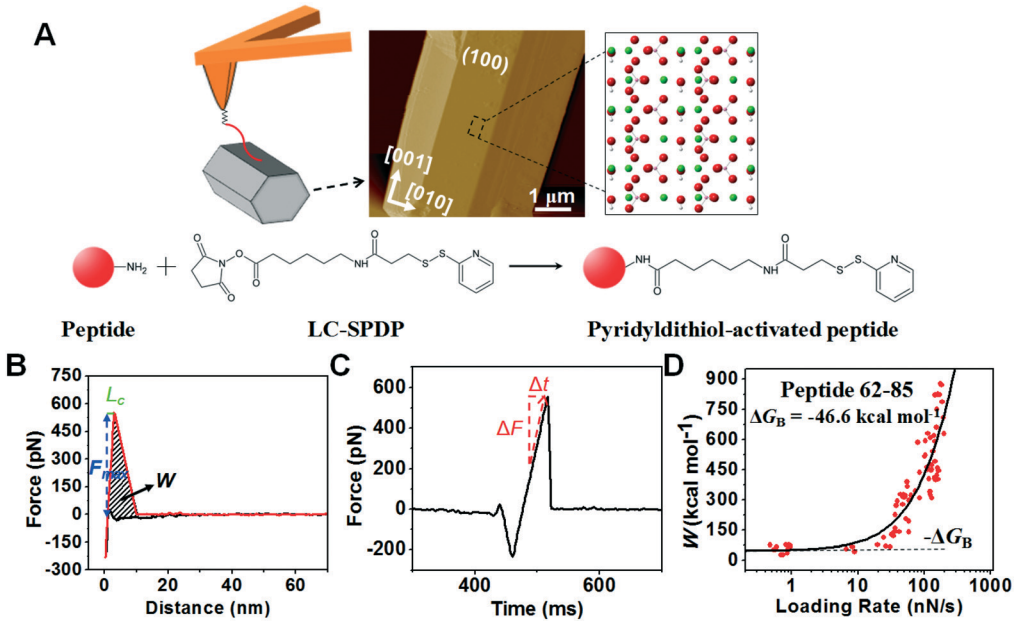

Fig. 8 Determination of the binding free energy for a single molecule of OPN peptide 62-85 on an HAP (100) face.[80] (A) A single-molecule of OPN peptide is linked to an Au-coated tip functionalized with cross-linker LC-SPDP. The modified AFM tip is forced to repeatedly approach and retreat from the HAP surface to obtain a series of (B) force–distance and (C) force–time curves. (D) Dynamic works (W) for rupturing the bonds between OPN peptide 62-85 and the HAP (100) face. Adapted with permission from ref. 80. Copyright 2017 American Chemical Society.

distance (F–d) curves.[79] Fig. 8B shows representative F–d curves associated with a single OPN peptide adsorbed onto a HAP (100) surface,[80] and analysis of the F–d curves allows the extraction of three parameters: the maximum adhesion force (F_{max}), the maximum pulling distance (L_c) and the total energy dissipation (W).[17,81] The F–d curves can be displayed as F–t curves (Fig. 8C), and the loading rate (r) can be calculated *via* the slope of F–t curves just prior to bond rupture.[17] Finally, the relationship between W and r can be fitted using a two-state theoretical model[17,82] to quantify the free-energy difference, ΔG_B. Since the process of bond rupture is time dependent, W is always larger than $-\Delta G_B$ ($W = -\Delta G_B$) and decreases gradually with the decrease of r.[17] When r is close to zero, W approaches $-\Delta G_B$, *i.e.*, the calculated binding free energy for OPN peptide 62-85 is −46.6 ± 11.5 kcal mol^{-1} (Fig. 8D).[80] The binding free energies −208 ± 36 and −179 ± 29 kcal mol^{-1} of collagen–HAP (100) and (110) faces, respectively, could be explained as different Ca^{2+} arrangements in different faces.[79] This suggests the presence of a better stereochemical relationship between collagen and the HAP (100) face.[79]

Except for the direct determination of protein or peptide–mineral interactions by SMFS with a combination of theoretical simulations, other methods such as sum-frequency generation (SFG)[83] can also characterize the detailed local structures and interactions of biomolecules at mineral interfaces.

6. Conclusions and perspectives

Ca-P-based calcified tissues are multifunctional and hierarchically organized. Understanding the nucleation and surface growth dynamics of Ca-Ps and their modulation by biomolecules can unveil the complicated biomineralization mechanisms. (1) We summarize the typical features of several Ca-Ps that could be imaged by *in situ* AFM and their surface growth dynamics by either the classical pathway or a nonclassical mechanism. (2) We present unique roles of soluble proteins, peptides and other organic molecules in Ca-P mineralization, and (3) we demonstrate the SMFS technique, which provides a thermodynamic basis for understanding protein–Ca-P mineral interactions. However, further AFM studies are needed:

(1) Scanning speed enhancement. Compared with conventional AFM imaging, high-speed AFM can significantly reduce imaging time by 100 to 1000 times.[84] This provides corroborative 'visual evidence' for the transient action of the protein–Ca-P mineral interaction and the dynamic behavior of biomolecules on mineral surfaces.

(2) Temperature. Mineralization of bones and teeth commonly proceeds at the physiological temperature of 37 °C, but most AFM studies are conducted at room temperature. The increase of temperature results in a faster step speed. This can be attributed to both the kinetic changes of adsorption and desorption rates of biomolecules on crystal surfaces and the thermodynamic changes of step free energies and overcoming the activation energy barrier. The revised dynamics will improve the understanding of the Ca-P mineralization mechanisms.

(3) Imaging soft substrates. Imaging Ca-P crystallization on soft substrates, such as cell membranes, provides technical support to observe biomolecule-regulated extracellular mineralization in physiological environments.

Conflicts of interest

There are no conflicts to declare.

Acknowledgements

This work was supported by the National Natural Science Foundation of China (41471245 and 41071208) and the Fundamental Research Funds for the Central Universities (2662017PY061 and 2662015PY206). C. V. P. acknowledges funding from the EU Seventh Framework Marie S. Curie ITNs: Minsc; CO_2 react; and Flowtrans.

References

1 S. Mann, *Biomineralization: principles and concepts in bioinorganic materials chemistry*. Oxford University Press, New York, 2001.
2 S. Weiner and L. Addadi, *J. Mater. Chem.*, 1997, **7**, 689–702.
3 L. J. Wang and G. H. Nancollas, *Chem. Rev.*, 2008, **108**, 4628–4669.
4 F. Betts and A. S. Posner, *Mater. Res. Bull.*, 1974, **9**, 353–360.
5 A. S. Posner and F. Betts, *Acc. Chem. Res.*, 1975, **8**, 273–281.
6 L. J. Wang, S. Y. Li, E. Ruiz-Agudo, C. V. Putnis and A. Putnis, *CrystEngComm*, 2012, **14**, 6252–6256.
7 B. Q. Xie, T. J. Halter, B. M. Borah and G. H. Nancollas, *Cryst. Growth Des.*, 2014, **14**, 1659–1665.
8 Q. Zhang, Y. Jiang, B. D. Gou, J. Huang, Y. X. Gao, J. T. Zhao, L. Zheng, Y. D. Zhao, T. L. Zhang and K. Wang, *Cryst. Growth Des.*, 2015, **15**, 2204–2210.
9 W. J. E. M. Habraken, J. H. Tao, L. J. Brylka, H. Friedrich, L. Bertinetti, A. S. Schenk, A. Verch, V. Dmitrovic, P. H. H. Bomans, P. M. Frederik, J. Laven, P. van der Schoot, B. Aichmayer, G. de With, J. J. De Yoreo and N. A. J. M. Sommerdijk, *Nat. Commun.*, 2013, **4**, 1507.
10 G. Mancardi, U. Terranova and N. H. De Leeuw, *Cryst. Growth Des.*, 2016, **16**, 3353–3358.
11 A. Dey, P. H. H. Bomans, F. A. Müller, J. Will, P. M. Frederik, G. de With and N. A. J. M. Sommerdijk, *Nat. Mater.*, 2010, **9**, 1010–1014.
12 M. Li, L. J. Wang, W. J. Zhang, C. V. Putnis and A. Putnis, *Cryst. Growth Des.*, 2016, **16**, 4509–4518.
13 H. H. Teng, P. M. Dove, C. A. Orme and J. J. De Yoreo, *Science*, 1998, **282**, 724–727.
14 C. M. Pina, U. Becker, P. Risthaus, D. Bosbach and A. Putnis, *Nature*, 1998, **395**, 483–486.
15 M. Rief, M. Gautel, F. Oesterhelt, J. M. Fernandez and H. E. Gaub, *Science*, 1997, **276**, 1109–1112.
16 G. E. Fantner, T. Hassenkam, J. H. Kindt, J. H. Weaver, H. Birkedal, L. Pechenik, J. A. Cutroni, G. A. Cidade, G. D. Stucky, D. E. Morse and P. K. Hansma, *Nat. Mater.*, 2005, **4**, 612–616.
17 R. W. Friddle, K. Battle, V. Trubetskoy, J. H. Tao, E. A. Salter, J. Moradian-Oldak, J. J. De Yoreo and A. Wierzbicki, *Angew. Chem., Int. Ed.*, 2011, **50**, 7541–7545.
18 S. V. Dorozhkin and M. Epple, *Angew. Chem., Int. Ed.*, 2002, **41**, 3130–3146.
19 S. R. Qiu and C. A. Orme, *Chem. Rev.*, 2008, **108**, 4784–4822.
20 M. Ohta, M. Tsutsumi and S. Ueno, *J. Cryst. Growth*, 1979, **47**, 135–136.
21 L. Scudiero, S. C. Langford and J. T. Dickinson, *Tribol. Lett.*, 1999, **6**, 41–55.
22 L. H. Qin, W. J. Zhang, J. W. Lu, A. G. Stack and L. J. Wang, *Environ. Sci. Technol.*, 2013, **47**, 13365–13374.
23 R. K. Tang, M. Darragh, C. A. Orme, X. Y. Guan, J. R. Hoyer and G. H. Nancollas, *Angew. Chem., Int. Ed.*, 2005, **44**, 3698–3702.
24 S. Y. Li, S. S. Wu, D. F. Nan, W. J. Zhang and L. J. Wang, *Chem. Mater.*, 2014, **26**, 5605–5612.
25 W. E. Brown, J. P. Smith, J. R. Lehr and A. W. Frazier, *Nature*, 1962, **196**, 1050–1055.
26 W. E. Brown, *Clin. Orthop. Relat. Res.*, 1966, **44**, 205–220.
27 R. Z. LeGeros, *Calcif. Tissue Int.*, 1985, **37**, 194–197.
28 K. Onuma and M. Iijima, *J. Cryst. Process Technol.*, 2015, **5**, 1–8.
29 S. S. Wu, M. H. Yu, M. Li, L. J. Wang, C. V. Putnis and A. Putnis, *Cryst. Growth Des.*, 2017, **17**, 2194–2202.
30 W. E. Brown, *Nature*, 1962, **196**, 1048–1050.
31 D. R. Taves, *Nature*, 1963, **200**, 1312–1313.
32 R. A. Terpstra and P. Bennema, *J. Cryst. Growth*, 1987, **82**, 416–426.
33 Y. H. Tseng, C. Y. Mou and J. C. C. Chan, *J. Am. Chem. Soc.*, 2006, **128**, 6909–6918.
34 I. Y. Pieters, E. A. P. De Maeyer and R. M. H. Verbeeck, *Inorg. Chem.*, 1996, **35**, 5791–5797.
35 I. Y. Pieters, E. A. P. De Maeyer and R. M. H. Verbeeck, *Inorg. Chem.*, 1998, **37**, 6392–6395.
36 M. I. Kay, R. A. Young and A. S. Posner, Crystal structure of hydroxyapatite, *Nature*, 1964, **204**, 1050–1052.
37 J. C. Elliott, P. E. Mackie and R. A. Young, Monoclinic hydroxyapatite, *Science*, 1973, **180**, 1055–1057.
38 J. C. Elliott, *Structure and chemistry of the apatites and other calcium orthophosphates*, Elsevier, 2013.
39 T. Kawasaki, M. Niikura and Y. Kobayashi, *J. Chromatogr. A*, 1990, **515**, 125–148.
40 N. H. De Leeuw and J. A. L. Rabone, *CrystEngComm*, 2007, **9**, 1178–1186.
41 K. Onuma and A. Ito, *Chem. Mater.*, 1998, **10**, 3346–3351.
42 W. K. Burton, N. Cabrera and F. C. Frank, *Philos. Trans. R. Soc., A*, 1951, **243**, 299–358.
43 J. P. Sizemore and M. F. Doherty, *Cryst. Growth Des.*, 2009, **9**, 2637–2645.
44 J. J. De Yoreo and P. G. Vekilov, *Rev. Mineral. Geochem.*, 2003, **54**, 57–93.
45 A. A. Chernov, *Phys.-Usp.*, 1961, **4**, 116–148.
46 K. Sangwal, *Prog. Cryst. Growth Charact. Mater.*, 1998, **36**, 163–248.
47 K. Onuma, *Prog. Cryst. Growth Charact. Mater.*, 2006, **52**, 223–245.
48 K. N. Olafson, M. A. Ketchum, J. D. Rimer and P. G. Vekilov, *Cryst. Growth Des.*, 2015, **15**, 5535–5542.
49 N. Kanzaki, K. Onuma, G. Treboux and A. Ito, *J. Cryst. Growth*, 2002, **235**, 465–470.

50 S. Elhadj, J. J. De Yoreo, J. R. Hoyer and P. M. Dove, *Proc. Natl. Acad. Sci. U. S. A.*, 2006, **103**, 19237–19242.
51 L. J. Wang, J. W. Lu, F. S. Xu and F. S. Zhang, *Chin. Sci. Bull.*, 2010, **55**, 2794–2802.
52 P. G. Vekilov, *Cryst. Growth Des.*, 2007, **7**, 2796–2810.
53 J. P. Sizemore and M. F. Doherty, *J. Cryst. Growth*, 2010, **312**, 785–792.
54 P. G. Vekilov, Y. G. Kuznetsov and A. A. Chernov, *J. Cryst. Growth*, 1992, **121**, 643–655.
55 P. W. Voorhees, *J. Stat. Phys.*, 1985, **38**, 231–252.
56 H. Zhang, J. J. De Yoreo and J. F. Banfield, *ACS Nano*, 2014, **8**, 6526–6530.
57 J. Christoffersen, E. Rostrup and M. R. Christoffersen, *J. Cryst. Growth*, 1991, **113**, 599–605.
58 A. J. Bray, *Adv. Phys.*, 2002, **51**, 481–587.
59 W. J. Wu and G. H. Nancollas, *Adv. Colloid Interface Sci.*, 1999, **79**, 229–279.
60 J. J. De Yoreo, P. U. Gilbert, N. A. J. M. Sommerdijk, R. L. Penn, S. Whitelam, D. Joester, H. Zhang, J. D. Rimer, A. Navrotsky, J. F. Banfield, A. F. Wallace, F. M. Michel, F. C. Meldrum, H. Cölfen and P. M. Dove, *Science*, 2015, **349**, aaa6760.
61 M. H. Nielsen, S. Aloni and J. J. De Yoreo, *Science*, 2014, **345**, 1158–1162.
62 M. H. Nielsen, D. Li, H. Zhang, S. Aloni, T. Y. J. Han, C. Frandsen, J. Seto, J. F. Banfield, H. Cölfen and J. J. De Yoreo, *Microsc. Microanal.*, 2014, **20**, 425–436.
63 C. Ruiz-Agudo, E. Ruiz-Agudo, C. V. Putnis and A. Putnis, *Cryst. Growth Des.*, 2015, **15**, 3724–3733.
64 H. Miura and R. Kobayashi, *Cryst. Growth Des.*, 2015, **15**, 2165–2175.
65 J. Chung, I. Granja, M. G. Taylor, G. Mpourmpakis, J. R. Asplin and J. D. Rimer, *Nature*, 2016, **536**, 446–450.
66 E. Ruiz-Agudo, C. V. Putnis, L. J. Wang and A. Putnis, *Geochim. Cosmochim. Acta*, 2011, **75**, 3803–3814.
67 P. M. Dove, J. J. De Yoreo and K. J. Davis, *Inhibition of $CaCO_3$ crystallization by small molecules: the magnesium example. Solid-Fluid Interfaces to Nanostructural Engineering*, ed. X. Y. Liu and J. J. De Yoreo, Kluewer/Plenum Academic Press, New York, 2004, vol. II.
68 N. Cabrera, D. A. Vermilyea, R. H. Doremus, B. W. Roberts and D. Turnbull, *Growth and Perfection of Crystals*, Wiley, N Y, 1958, p. 393.
69 J. J. De Yoreo, L. A. Zepeda-Ruiz, R. W. Friddle, S. R. Qiu, L. E. Wasylenki, A. A. Chernov, G. H. Gilmer and P. M. Dove, *Cryst. Growth Des.*, 2009, **9**, 5135–5144.
70 S. Y. Potapenko, *J. Cryst. Growth*, 1993, **133**, 147–154.
71 L. J. Wang, J. J. De Yoreo, X. Guan, S. R. Qiu, J. R. Hoyer and G. H. Nancollas, *Cryst. Growth Des.*, 2006, **6**, 1769–1775.
72 T. A. Land, T. L. Martin, S. Potapenko, G. T. Palmore and J. J. De Yoreo, *Nature*, 1999, **399**, 442–445.
73 S. S. Wu, H. Zhai, W. J. Zhang and L. J. Wang, *Cryst. Growth Des.*, 2015, **15**, 4490–4497.
74 A. J. Giuffre, L. M. Hamm, N. Z. Han, J. J. De Yoreo and P. M. Dove, *Proc. Natl. Acad. Sci. U. S. A.*, 2013, **110**, 9261–9266.
75 S. Elhadj, J. J. De Yoreo, J. R. Hoyer and P. M. Dove, *Proc. Natl. Acad. Sci. U. S. A.*, 2006, **103**, 19237–19242.
76 Y. Y. Hu, A. Rawal and K. Schmidt-Rohr, *Proc. Natl. Acad. Sci. U. S. A.*, 2010, **107**, 22425–22429.
77 A. Adamiano, N. Sangiorgi, S. Sprio, A. Ruffini, M. Sandri, A. Sanson, P. Gras, D. Grossin, C. Frances, K. Chatzipanagis, M. Bilton, B. Marzec, A. Varesano, F. Meldrum, R. Kroger and A. Tampier, *J. Mater. Chem. B*, 2017, **5**, 7608–7621.
78 R. Merkel, P. Nassoy, A. Leung, K. Ritchie and E. Evans, *Nature*, 1999, **397**, 50–53.
79 J. H. Tao, K. C. Battle, H. H. Pan, E. A. Salter, Y. C. Chien, A. Wierzbicki and J. J. De Yoreo, *Proc. Natl. Acad. Sci. U. S. A.*, 2015, **112**, 326–331.
80 M. Li, L. J. Wang and C. V. Putnis, *J. Phys. Chem. B*, 2017, **121**, 5968–5976.
81 G. E. Fantner, J. Adams, P. Turner, P. J. Thurner, L. W. Fisher and P. K. Hansma, *Nano Lett.*, 2007, **7**, 2491–2498.
82 R. W. Friddle, *Phys. Rev. Lett.*, 2008, **100**, 138302.
83 B. Ding, J. Jasensky, Y. Li and Z. Chen, *Acc. Chem. Res.*, 2016, **49**, 1149–1157.
84 N. Kodera, D. Yamamoto, R. Ishikawa and T. Ando, *Nature*, 2010, **468**, 72–76.

